

# Grain rotation and lattice deformation during photoinduced chemical reactions revealed by *in situ* X-ray nanodiffraction

Zhifeng Huang<sup>1†</sup>, Matthias Bartels<sup>2</sup>, Rui Xu<sup>1</sup>, Markus Osterhoff<sup>2</sup>, Sebastian Kalbfleisch<sup>2</sup>, Michael Sprung<sup>3</sup>, Akihiro Suzuki<sup>4</sup>, Yukio Takahashi<sup>4</sup>, Thomas N. Blanton<sup>5†</sup>, Tim Salditt<sup>2</sup> and Jianwei Miao<sup>1\*</sup>

***In situ* X-ray diffraction (XRD) and transmission electron microscopy (TEM) have been used to investigate many physical science phenomena, ranging from phase transitions, chemical reactions and crystal growth to grain boundary dynamics<sup>1–6</sup>. A major limitation of *in situ* XRD and TEM is a compromise that has to be made between spatial and temporal resolution<sup>1–6</sup>. Here, we report the development of *in situ* X-ray nanodiffraction to measure high-resolution diffraction patterns from single grains with up to 5 ms temporal resolution. We observed, for the first time, grain rotation and lattice deformation in chemical reactions induced by X-ray photons:  $\text{Br}^- + h\nu \rightarrow \text{Br} + e^-$  and  $e^- + \text{Ag}^+ \rightarrow \text{Ag}^0$ . The grain rotation and lattice deformation associated with the chemical reactions were quantified to be as fast as  $3.25 \text{ rad s}^{-1}$  and as large as  $0.5 \text{ \AA}$ , respectively. The ability to measure high-resolution diffraction patterns from individual grains with a temporal resolution of several milliseconds is expected to find broad applications in materials science, physics, chemistry and nanoscience.**

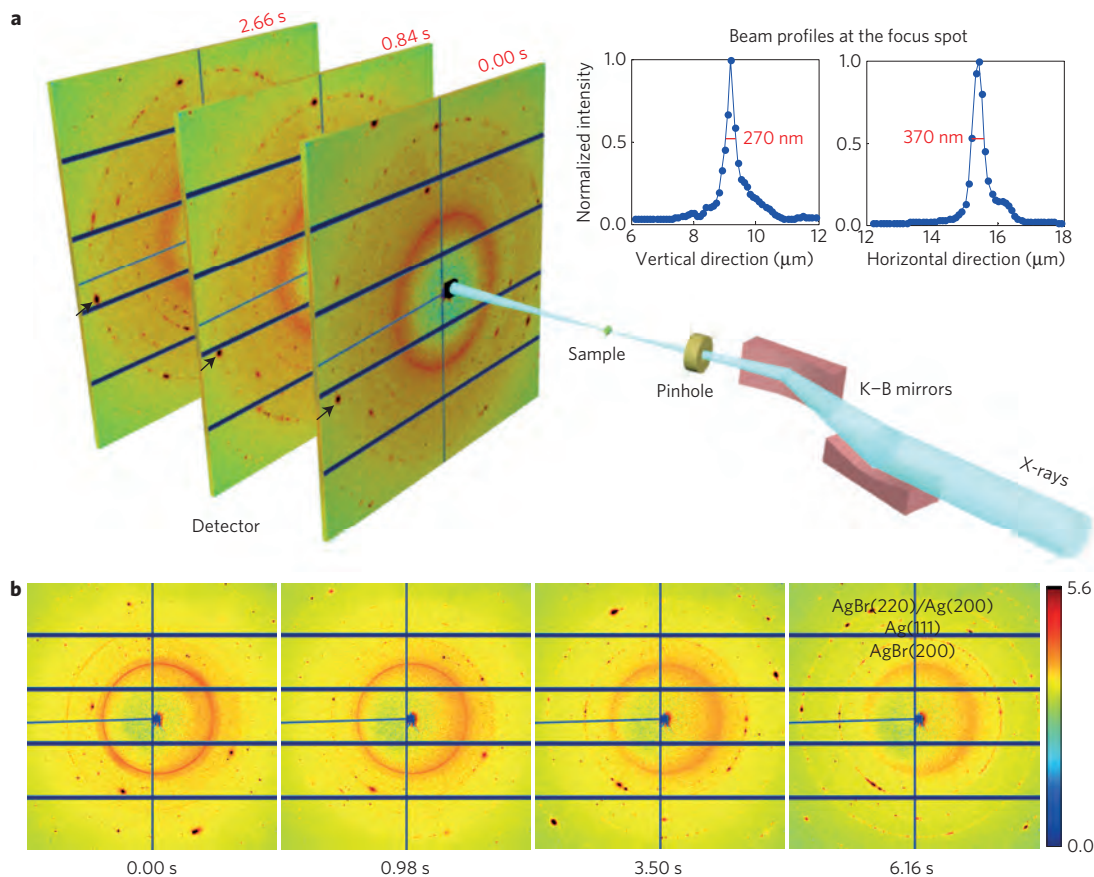
Many materials are polycrystalline and are made of a large number of grains of varying size and orientation. The structure and dynamics of grains and grain boundaries are thus fundamental to many material properties<sup>7,8</sup>. Several experimental methods can be used to characterize grains and grain boundaries in materials, including XRD, coherent diffractive imaging, TEM, electron tomography, scanning electron microscopy (SEM), electron diffraction and optical microscopy<sup>1–4,7–15</sup>. Although TEM and electron tomography can image grains and grain boundaries at atomic resolution<sup>10,14,15</sup>, their temporal resolutions are very limited<sup>5,6,11,16</sup>. *In situ* XRD can achieve better temporal resolution and is more flexible in sample environments, but only provides the ensemble-average structure of multiple grains<sup>2–4,13</sup>. Here, we demonstrated *in situ* X-ray nanodiffraction to measure high-resolution diffraction patterns from single grains with a temporal resolution of several milliseconds through a combination of a brilliant synchrotron undulator beam, Kirkpatrick–Baez (K–B) mirrors and a state-of-the-art X-ray detector (PILATUS). With this system, we performed first real-time measurements of grain rotation and lattice deformation during photoinduced chemical reactions with up to 5 ms temporal resolution.

Figure 1a shows the schematic layout of the *in situ* X-ray nanodiffraction instrument, utilizing at present the brightest synchrotron in the world—the positron–electron tandem ring accelerator (PETRA) III in Germany. Monochromatic X-rays with energy  $E = 13.8$  or  $13.6 \text{ keV}$  were focused to a spot of  $\sim 370 \text{ nm} \times 270 \text{ nm}$  by two K–B mirrors<sup>17</sup>. The sample was positioned at the focal spot with a flux of  $\sim 6.74 \times 10^{11}$  photons  $\text{s}^{-1}$ . Two detector configurations were implemented in the experiments. In the first configuration, a PILATUS 1M detector, consisting of ten modules, each with  $487 \times 195$  pixels and a pixel size of  $172 \times 172 \mu\text{m}^2$ , was placed at a distance of  $167.8 \text{ mm}$  downstream of the sample. The PILATUS detector has a dynamic range of 20 bits and single-photon sensitivity<sup>18</sup>. The readout time of PILATUS 1M is  $40 \text{ ms}$  in the full-frame mode,  $9 \text{ ms}$  in the three-module mode, and  $3 \text{ ms}$  in the single-module mode. In the second configuration, a PILATUS 6M detector of 60 modules was mounted at a distance of  $386.7 \text{ mm}$  from the sample. The readout time of PILATUS 6M is  $30 \text{ ms}$  in the full-frame mode. This instrument allowed us to measure high-resolution diffraction patterns with millisecond timescales from a  $\sim 370 \text{ nm} \times 270 \text{ nm}$  illumination area (Methods, Fig. 1 and Supplementary Fig. 1).

Using this *in situ* X-ray nanodiffraction system, we studied three groups of samples in an ambient environment at room temperature (Methods): Kodak direct print linagraph paper (Type 2167) containing AgBr, gelatin and other materials; AgBr control samples consisting of either AgBr powder on  $\text{Si}_3\text{N}_4$  membranes or AgBr/gelatin; and non-AgBr control samples consisting of  $\text{TiO}_2/\text{gelatin}$ ,  $\text{CeO}_2/\text{gelatin}$  or Ag/gelatin. Figure 1b and Supplementary Movie 1 show real-time measurements of the diffraction patterns from a Kodak linagraph paper during photoinduced chemical reactions ( $\text{Br}^- + h\nu \rightarrow \text{Br} + e^-$  and  $e^- + \text{Ag}^+ \rightarrow \text{Ag}^0$ ), initiated by exposing the sample to X-rays. In the Kodak paper, cubic AgBr grains with an average size of  $\sim 700 \text{ nm}$  were distributed in a layer near the surface (Supplementary Fig. 2). Because the size of the X-ray beam was smaller than the individual AgBr grain size (Methods), several large and high-intensity diffraction spots were initially diffracted from single AgBr grains. With further X-ray irradiation, the large AgBr(200) and (220) spots gradually became smaller and there was an increase in the number

<sup>1</sup>Department of Physics & Astronomy and California NanoSystems Institute, University of California, Los Angeles, California 90095, USA. <sup>2</sup>Institut für Röntgenphysik, Georg-August-Universität Göttingen, Friedrich-Hund-Platz 1, 37077 Göttingen, Germany. <sup>3</sup>DESY, Notkestr. 85, 22607 Hamburg, Germany. <sup>4</sup>Department of Precision Science and Technology, Graduate School of Engineering, Osaka University, 2-1 Yamada-oka, Suita, Osaka 565-0871, Japan. <sup>5</sup>Kodak Technology Center, Eastman Kodak Company, Rochester, New York 14650-2106, USA. †Present addresses: Carl ZEISS X-ray Microscopy Inc., Pleasanton, California 94588, USA (Z.H.); International Centre for Diffraction Data, Newtown Square, Pennsylvania 19073, USA (T.N.B.).

\*e-mail: miao@physics.ucla.edu



**Figure 1 | Schematic layout of *in situ* X-ray nanodiffraction with up to 5 ms temporal resolution. a**, Monochromatic X-rays were focused to a spot size of  $\sim 370 \text{ nm} \times 270 \text{ nm}$  (inset) by two K-B mirrors. A pinhole was used to remove the parasitic scattering from the K-B mirrors. The sample was positioned at the focal spot with a flux of  $\sim 6.74 \times 10^{11} \text{ photons s}^{-1}$ , and high-resolution diffraction patterns from the samples were collected by a PILATUS 1M or 6M detector. Three representative diffraction patterns were measured from a Kodak linagraph paper at 0, 0.84 and 2.66 s, respectively, in which diffraction spots (arrows) were rotating along the Debye–Scherrer rings. **b**, Real-time observation of the photolysis of AgBr grains to produce Ag nanograins. Four representative diffraction patterns were extracted from Supplementary Movie 1 at 0, 0.98, 3.50 and 6.16 s, respectively, which were collected by the PILATUS 1M detector (temporal resolution: 140 ms).

of diffraction spots, indicating the AgBr grains were decomposed into smaller grains. Meanwhile, Ag(111) and (200) diffraction spots appeared in the diffraction patterns, implying that Ag nanograins started nucleating and growing with the photolysis of the AgBr grains. After several seconds of X-ray exposure, the Debye–Scherrer rings of AgBr(200), (220), Ag(111) and (200) started to appear (Fig. 1b, Supplementary Fig. 3 and Supplementary Movie 1). These represent real-time measurements of the photolysis of AgBr to produce Ag (refs 19,20). This type of the photolysis was also observed by exposing controlled AgBr samples to the nanofocused X-rays (Supplementary Fig. 4 and Supplementary Movie 2). Compared to the controlled samples, the speed of the photolysis of AgBr in the Kodak paper was faster, owing to the chemical sensitization of photographic Ag halides grains (Supplementary Information), a more uniform distribution and smaller size of AgBr grains in the Kodak paper. For the controlled non-AgBr samples, we did not observe any motion of the diffraction spots.

Next, we investigated the occurrence of grain rotation during the photolysis of AgBr to produce Ag. As the PILATUS detector captured a cross-section of the Ewald sphere (that is, forming a Debye–Scherrer ring), evidence of the grain rotation was observed in both the Kodak linagraph paper and controlled AgBr samples (Supplementary Movies 1 and 2). To quantitatively analyse the grain rotation, we azimuthally plotted the intensity of the AgBr(200) and Ag(111) Debye–Scherrer rings as a function of the exposure time for Supplementary Movie 1 (Fig. 2a,b). Careful examination

of the figures indicates that there were three types of grain-related features: individual points, representing reciprocal lattice points momentarily intersecting the Ewald sphere; horizontal tracks, representing stationary diffraction spots and grains; and curved tracks along the Debye–Scherrer ring. In particular, some of the curved tracks were oblique lines, indicating a constant angular velocity of the grain rotation.

Although grain rotation due to external load or during grain growth has been described before<sup>3,11,16,21,22</sup>, in this study we observed grain rotation during chemical reactions that has not been previously reported. According to photographic theory<sup>19,20</sup> (Supplementary Information), point defects and dislocations in AgBr grains act as sensitized sites for Ag nucleation and aggregation. Unlike visible light, which produces one Ag atom per absorbed light photon, an absorbed X-ray photon can produce many photolytic Ag atoms<sup>19</sup>, which can grow and agglomerate on the surfaces of and inside a AgBr grain. As latent imaging sites grow in size owing to inhomogeneous nucleation of Ag atom agglomeration inside the AgBr grain, stress is built up. With the growth of Ag nanograins, the resulting strain exceeds elastic deformation and the AgBr grain can fragment into smaller grains, which drives the grain rotation. Figure 2c shows a major AgBr(200) spot decomposed into smaller spots. SEM images of both the Kodak linagraph paper and controlled AgBr samples confirmed the fragmentation of AgBr grains and the existence of filamentary Ag structure on the surface of the grains after X-ray exposure (Supplementary Fig. 5), which is

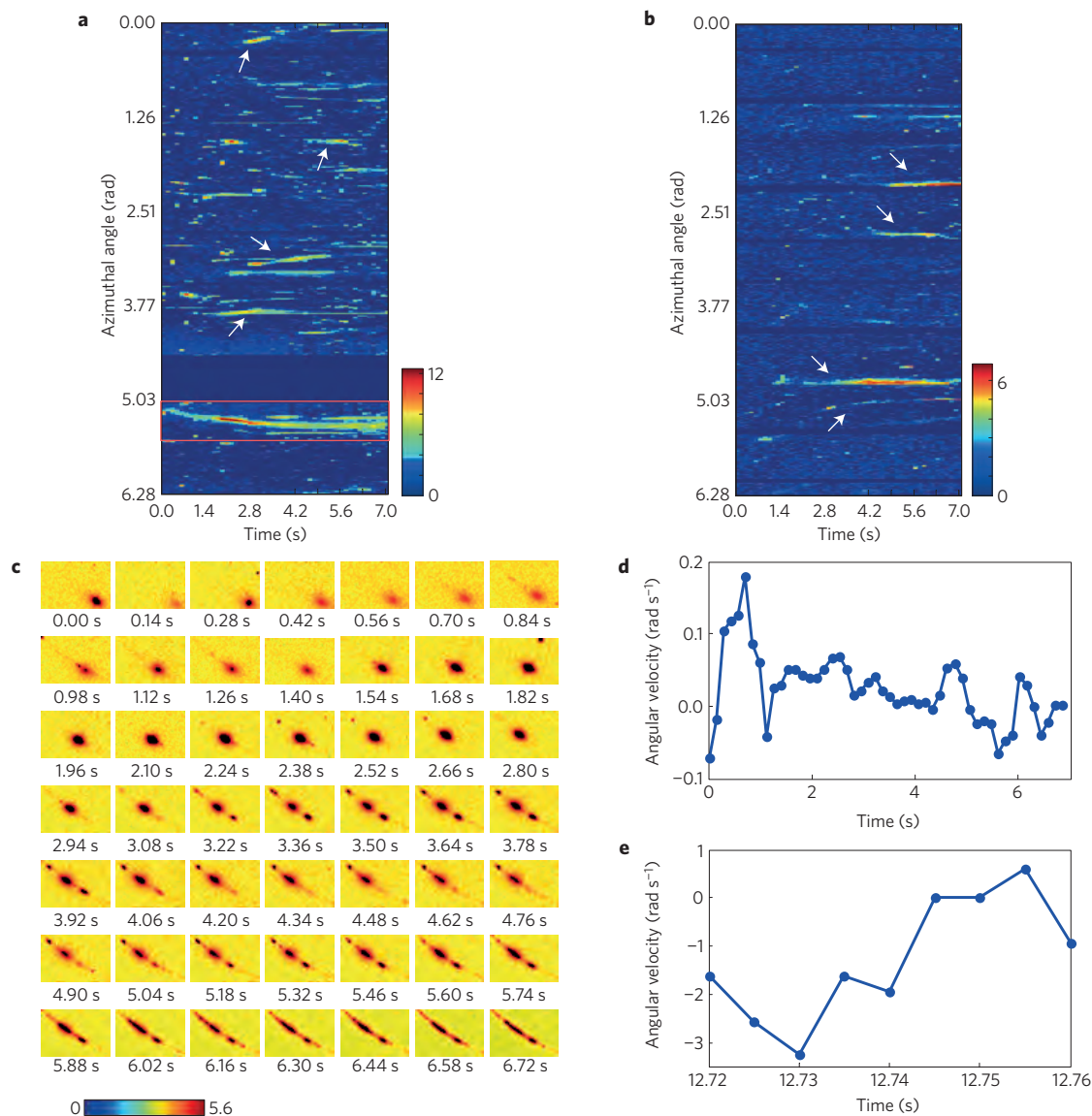


**Figure 2 | Real-time observation of grain rotation in chemical reactions induced by X-ray photons.** **a, b**, Azimuthal plot of the diffraction intensity of the AgBr(200) (**a**) and Ag(111) (**b**) Debye-Scherrer rings as a function of the exposure time for Supplementary Movie 1 (temporal resolution: 140 ms), measured from a Kodak linagraph paper. Three types of grain-related features were observed: individual points; horizontal tracks; and curved tracks along the Debye-Scherrer ring (arrows). **c**, A sequence of images of the rectangular region in **a**, showing a major AgBr(200) spot fragmented into smaller spots. **d**, Measurements of the angular velocity of a major diffraction spot in **c** as a function of the exposure time. **e**, Measurements of the angular velocity of a diffraction spot in Supplementary Movie 3 as a function of the exposure time (temporal resolution: 5 ms), in which the fastest instantaneous angular velocity was  $3.25 \text{ rad s}^{-1}$ .

also consistent with post light exposure studies of Ag halides<sup>23,24</sup>. With the release of the internal stress, the angular velocity of the major diffraction spot gradually slows down as a function of the exposure time (Fig. 2d) and eventually becomes stable (Fig. 2a). In the experiments of this study, the angular velocity of the grain rotation was measured to be as fast as  $3.25 \text{ rad s}^{-1}$  (Fig. 2e and Supplementary Movie 3), which is significantly faster than that of previously reported grain rotation<sup>3,11,16,21,22</sup>.

In addition to grain rotation, lattice deformation was also observed during the X-ray exposure of the Kodak linagraph paper and controlled AgBr samples. Real-time measurements of simultaneous grain rotation and lattice deformation in photolysis of AgBr to produce Ag grains are shown in Fig. 3, Supplementary Figs 6 and 7 and Supplementary Movies 4–8. In our experiments, three types of Ag lattice deformation were observed. The first was related to the fragmentation of AgBr grains (Fig. 2c), requiring lattice

deformation and stress build-up of the internal Ag nanograins. The second was irregular lattice deformation, that is, diffraction spots oscillated irregularly around the Ag Debye-Scherrer rings. Figure 3b and Supplementary Movie 4 show a diffraction spot initially observed with a lattice spacing of  $2.36 \text{ \AA}$ , which is close to the Ag(111) reflection. The spot then quickly moved to a lower  $2\theta$  direction (indicating lattice expansion). After the lattice spacing reached a maximum of  $2.40 \text{ \AA}$ , the diffraction spot reversed its direction and moved to a higher  $2\theta$  direction (lattice contraction). After  $1.36 \text{ s}$  the lattice spacing reached a minimum of  $2.31 \text{ \AA}$  and then the diffraction spot moved back to the Ag(111) ring again (lattice expansion) until the spot finally disappeared on the detector plane. The time span of the whole lattice deformation process was  $2.29 \text{ s}$ , which was simultaneously accompanied by grain rotation. Figure 3e shows the lattice spacing, the corresponding normal component strain, and the angular distribution of the diffraction

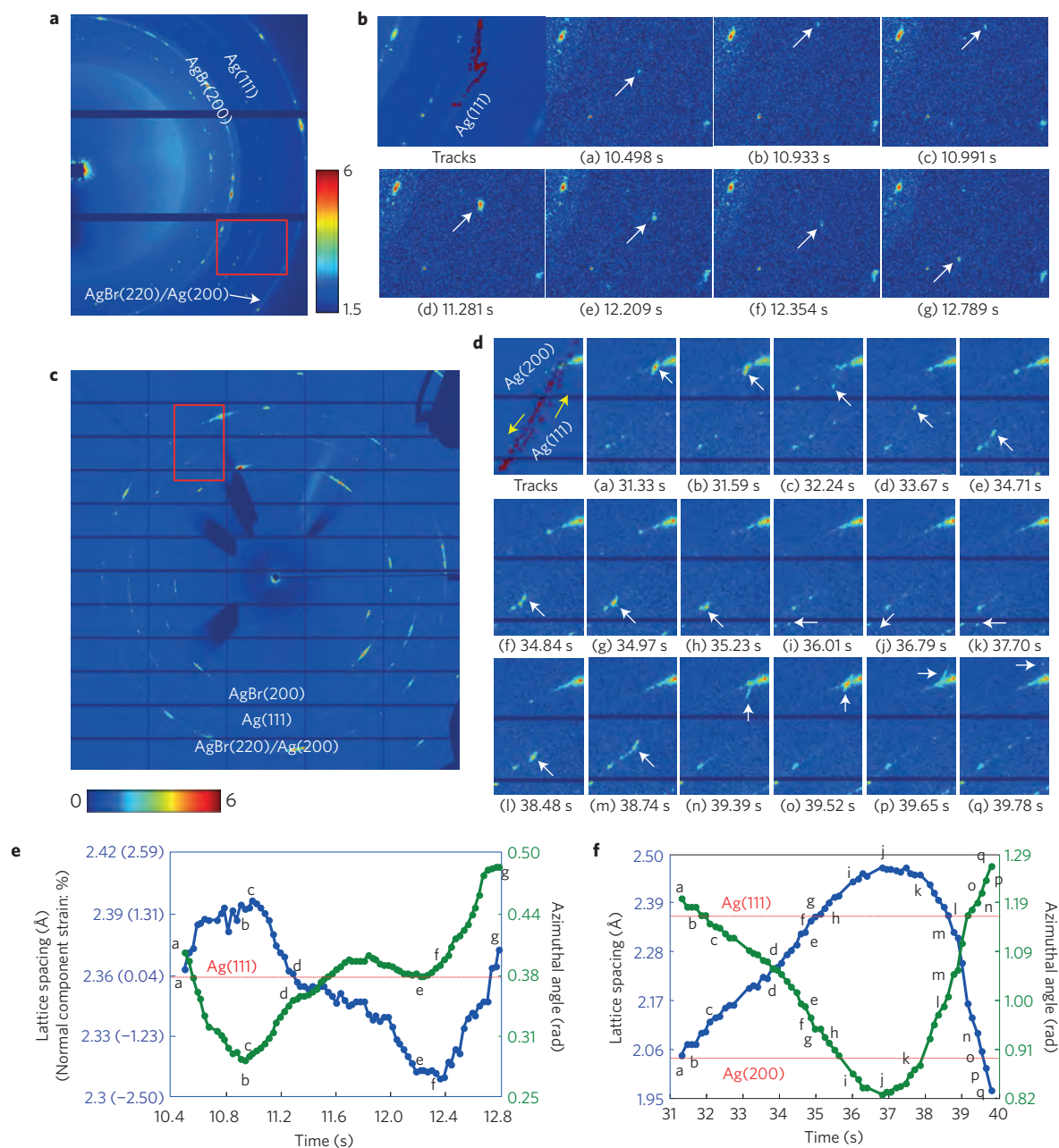


**Figure 3 | Real-time observation of simultaneous grain rotation and lattice deformation in chemical reactions induced by X-ray photons.** **a**, Diffraction intensity averaged from real-time measurements of another Kodak linagraph paper (Supplementary Movies 4 and 5, temporal resolution: 29 ms). **b**, A track image and seven representative frames of the rectangular region in **a** extracted from Supplementary Movie 4. The track image shows the trajectory of a moving diffraction spot between 10.50 and 12.79 s, where arrows show the motion of the diffraction spot. **c**, Diffraction intensity averaged from real-time measurements of a controlled AgBr/membrane sample (Supplementary Movie 6, temporal resolution: 130 ms). **d**, A track image and 18 representative frames of the rectangular region in **c** extracted from Supplementary Movie 6. The track image shows the trajectory of a diffraction spot between 31.33 and 39.78 s, where arrows show the motion of the diffraction spot. **e**, Quantification of the lattice deformation, normal component strain and grain rotation of the rectangular region in **a** between 10.50 and 12.79 s, where labels a–g correspond to those in **b**. **f**, Quantification of the lattice deformation and grain rotation of the rectangular region in **c** between 31.33 and 39.78 s, where labels a–q correspond to those in **d**.

spot as a function of the exposure time. The normal component strain was determined to be in the range from  $-2.12$  to  $+1.61\%$  in this example.

The third type showed more significant lattice deformation, that is, the tracks of diffraction spots formed straight or curved lines across the Ag(111) and (200) Debye–Scherrer rings. Figure 3d and Supplementary Movie 6 show a diffraction spot initiating on the Ag(200) ring and moving in a straight line towards inside the Ag(111) ring, which corresponds to a lattice expansion of  $0.42 \text{ \AA}$ .

The diffraction spot then moved from inside the Ag(111) ring towards outside the Ag(200) ring, corresponding to a lattice contraction of  $0.5 \text{ \AA}$  (Fig. 3f). The whole process of the photoinduced lattice deformation lasted 8.45 s and the magnitude of the lattice deformation was significantly larger than those previously reported<sup>25–28</sup>. Like the second type (Fig. 3e), the third type of lattice deformation was also simultaneously accompanied by grain rotation (Fig. 3f). Similar tracks are also shown in Supplementary Figs 6 and 7 and Supplementary Movies 5, 7 and 8. As Ag atoms aggregate to form

nanoparticles at the latent imaging sites inside a AgBr grain, the lattice structure of newly formed Ag nanograins is generally unstable<sup>29</sup> and consists of structural defects<sup>30</sup>. Previous studies showed that the presence of stacking faults and twin planes in face-centred cubic Ag lattice can generate hexagonal close-packed lamellae and produce the Ag(1100) lattice spacing of 2.49 Å (refs 30,31), which is very close to the lattice spacing observed in our experiment (point j in Fig. 3f). Thus the significant lattice deformation presented in our experimental data (Fig. 3f) is probably due to the crystal structure changes of the unstable Ag nanograins<sup>30,31</sup>.

In conclusion, we have developed *in situ* X-ray nanodiffraction with up to 5 ms temporal resolution, and performed first real-time measurements of the grain rotation and lattice deformation in photoinduced chemical reactions. As both advanced synchrotron light sources and X-ray optics are at present under rapid development worldwide<sup>9</sup>, the focal spot of the *in situ* X-ray nanodiffraction system can be further improved to the ~10 nm level<sup>32</sup>, allowing the study of the subgrain dynamics in materials. We thus anticipate that such an *in situ* X-ray nanodiffraction technique will find broad applications across several disciplines.

## Methods

Methods and any associated references are available in the [online version of the paper](#).

Received 8 September 2014; accepted 30 April 2015;  
published online 8 June 2015

## References

- Reimers, J. N. & Dahn, J. R. Electrochemical and *in situ* X-ray diffraction studies of lithium intercalation in  $\text{Li}_x\text{CoO}_2$ . *J. Electrochem. Soc.* **139**, 2091–2097 (1992).
- Grossa, K. J., Guthrie, S., Takara, S. & Thomas, G. *In-situ* X-ray diffraction study of the decomposition of  $\text{NaAlH}_4$ . *J. Alloys Compd.* **297**, 270–281 (2000).
- Margulies, L., Winther, G. & Poulsen, H. F. *In situ* measurement of grain rotation during deformation of polycrystals. *Science* **291**, 2392–2394 (2001).
- Schmidt, S. *et al.* Watching the growth of bulk grains during recrystallization of deformed Metals. *Science* **305**, 229–232 (2004).
- Williamson, M. J., Tromp, R. M., Vereecken, P. M., Hull, R. & Ross, F. M. Dynamic microscopy of nanoscale cluster growth at the solid–liquid interface. *Nature Mater.* **2**, 532–536 (2003).
- Zheng, H. *et al.* Observation of single colloidal platinum nanocrystal growth trajectories. *Science* **324**, 1309–1312 (2009).
- Gottstein, G. & Shvindlerman, L. S. *Grain Boundary Migration in Metals: Thermodynamics, Kinetics, Applications* 2nd edn (CRC Press, 2009).
- Hull, D. & Bacon, D. J. *Introduction to Dislocations* 5th edn (Butterworth-Heinemann, 2011).
- Miao, J., Ishikawa, T., Robinson, I. K. & Murnane, M. M. Beyond crystallography: Diffractive imaging using coherent X-ray light source. *Science* **348**, 530–535 (2015).
- Williams, D. B. & Carter, C. B. *Transmission Electron Microscopy: A Textbook for Materials Science* 2nd edn (Springer, 2009).
- Ke, M., Hackney, S. A., Milligan, W. W. & Aifantis, E. C. Observation and measurement of grain rotation and plastic strain in nanostructured metal thin films. *Nanostruct. Mater.* **5**, 689–697 (1995).
- Larson, B. C., Yang, W., Ice, G. E., Budai, J. D. & Tischler, J. Z. Three-dimensional X-ray structural microscopy with submicrometre resolution. *Nature* **415**, 887–890 (2002).
- Offerman, S. E. *et al.* Grain nucleation and growth during phase transformations. *Science* **298**, 1003–1005 (2002).
- Scott, M. C. *et al.* Electron tomography at 2.4-Å resolution. *Nature* **483**, 444–447 (2012).
- Chen, C.-C. *et al.* Three-dimensional imaging of dislocations in a nanoparticle at atomic resolution. *Nature* **496**, 74–77 (2013).
- Harris, K. E., Singh, V. V. & King, A. H. Grain rotation in thin films of gold. *Acta Mater.* **46**, 2623–2633 (1998).
- Salditt, T. *et al.* Partially coherent nano-focused x-ray radiation characterized by Talbot interferometry. *Opt. Express* **19**, 9656–9675 (2011).
- Kraft, P. *et al.* Performance of single-photon-counting PILATUS detector modules. *J. Synchrotron Radiat.* **16**, 368–375 (2009).
- James, T. H. (ed.) *The Theory of the Photographic Process* 4th edn (Macmillan Publishing Co., 1977).
- Gurney, R. W. & Mott, N. F. The theory of the photolysis of silver bromide and the photographic latent image. *Proc. R. Soc. Lond. A* **64**, 151–167 (1938).
- Leite, E. R. *et al.* Crystal growth in colloidal tin oxide nanocrystals induced by coalescence at room temperature. *Appl. Phys. Lett.* **83**, 1566–1568 (2003).
- Shan, Z. *et al.* Grain boundary-mediated plasticity in nanocrystalline nickel. *Science* **305**, 654–657 (2004).
- Berry, C. R. & Griffith, R. L. Structure and growth mechanism of photolytic silver in silver bromide. *Acta Crystallogr.* **3**, 219–222 (1950).
- Burley, G. Photolytic behavior of silver iodide. *J. Res. Natl Bur. Stand.* **67A**, 301–307 (1963).
- Pearson, W. B. *A Handbook of Lattice Spacings and Structures of Metals and Alloys* (Pergamon Press, 1958).
- Huberman, M. L. & Grimsditch, M. Lattice expansions and contractions in metallic superlattices. *Phys. Rev. Lett.* **62**, 1403–1406 (1989).
- Diao, J., Gall, K. & Dunn, M. L. Surface-stress-induced phase transformation in metal nanowires. *Nature Mater.* **2**, 656–660 (2003).
- Clark, J. N. *et al.* Ultrafast three-dimensional imaging of lattice dynamics in individual gold nanocrystals. *Science* **341**, 56–59 (2013).
- Shyjumon, I. *et al.* Structural deformation, melting point and lattice parameter studies of size selected silver clusters. *Eur. Phys. J. D* **37**, 409–415 (2006).
- Rocha, T. C. R. & Zanchet, D. Structural defects and their role in the growth of Ag triangular nanoplates. *J. Phys. Chem. C* **111**, 6989–6993 (2007).
- Kirkland, A. I. *et al.* Structural studies of trigonal lamellar particles of gold and silver. *Proc. R. Soc. Lond. A* **440**, 589–609 (1993).
- Ice, G. E., Budai, J. D. & Pang, J. W. L. The race to X-ray microbeam and nanobeam science. *Science* **334**, 1234–1239 (2011).

## Acknowledgements

We thank I. Vartanians for stimulating discussions and A. Zozulya for help with the experiments. This work was supported by the DARPA PULSE program through a grant from AMRDEC and Helmholtz Society grants VH-VI-403 and DFG SFB755. This work was also partially funded by the Office of Basic Energy Sciences of the US Department of Energy (Grant No. DE-FG02-13ER46943), ONR MURI (Grant No. N00014-14-1-0675) and NSF (Grant No. DMR-1437263).

## Author contributions

J.M. directed the project; Z.H., M.B., R.X., T.S., J.M., M.O., S.K., M.S., A.S., Y.T. and T.N.B. conducted the experiments; Z.H., J.M., M.B., T.N.B., T.S. and M.S. performed the data analysis; J.M., Z.H., T.S. and T.N.B. wrote the manuscript.

## Additional information

Supplementary information is available in the [online version of the paper](#). Reprints and permissions information is available online at [www.nature.com/reprints](http://www.nature.com/reprints). Correspondence and requests for materials should be addressed to J.M.

## Competing financial interests

The authors declare no competing financial interests.

## Methods

**Sample preparation.** Group #1: Kodak direct print linagraph paper. Kodak direct print linagraph paper (Type 2167) turns to light grey after exposure to visible light, and turns to black after exposure to X-rays. The Kodak linagraph paper uses cellulose Type Ib as the support and gelatin as the coating binder, and contains talc (paper transport aid), hydrotalcite (paper transport aid), rutile TiO<sub>2</sub> (filler), polyethylene (overcoat) and AgBr (photosensitive component). An XRD phase analysis of the linagraph paper measured with a Cu rotating anode X-ray generator is shown in Supplementary Fig. 3b.

Group #2: AgBr control samples. All AgBr control samples were made under low-light conditions to reduce the amount of Ag print out.

AgBr/membrane. Into a glass beaker was added 50 ml deionized (DI) water and 3.167 g AgNO<sub>3</sub> (Eastman Kodak Company). Into a second beaker was added 50 ml DI water and 2.124 g NaBr (MCB Chemical). The AgNO<sub>3</sub> solution was added dropwise to the NaBr solution while stirring with a magnetic stir bar. A precipitate immediately formed. The resulting dispersion was allowed to stir for 15 min and was then vacuum filtered using a Millipore RA filter (1.2 μm). The collected solids were transferred to a glass dish and dried for 30 min at 100 °C. XRD identified the dried powder as AgBr. The AgBr powder was mixed with distilled water, and a droplet of solution was placed on silicon nitride membranes. The membranes were air dried before *in situ* XRD experiments.

AgBr/gelatin. Into a glass beaker was added 75 ml DI water and 0.45 g AgNO<sub>3</sub>. Into a second beaker was added 50 ml DI water and 0.29 g NaBr. The AgNO<sub>3</sub> solution was added dropwise to the NaBr solution while stirring with a magnetic stir bar. A precipitate immediately formed. The resulting dispersion was allowed to stir for 15 min and was then centrifuged. The liquid centrifugate was poured off, DI water added, sonicated and the centrifuge process was repeated. To the remaining solids in the centrifuge tube was added 10 ml of a 5 wt% Type 40 gelatin (Eastman Gelatin) aqueous solution (gelatin solution at 40 °C). The solution was sonicated and then poured into a glass beaker, while kept at 40 °C and stirred using a magnetic stir bar. Horiba analysis found the median AgBr particle size to be ~0.134 μm and an XRD experiment confirmed the particles to be AgBr. AgBr/gelatin samples for this study were prepared as free-standing films or on a filter. An aliquot of the AgBr–gelatin dispersion was puddle deposited onto an unsubbed poly(ethylene terephthalate) (PET) support. A draw bar with a 200 μm gap was used to produce a wet coating of the dispersion on the PET. The coating dried in ambient air, and was removed from the PET, resulting in a free-standing AgBr–gelatin film. A 4 ml aliquot of the AgBr–gelatin dispersion from above was vacuum filtered using a Millipore VM filter (0.05 μm). The collected sample was washed with 100 ml of 40 °C DI water to remove most of the gelatin. The filter with the AgBr coating was removed from the filter apparatus and allowed to dry in ambient air.

Group #3: non-AgBr control samples. These samples were used to confirm that the grain rotation and lattice deformation observed are not due to gelatin.

TiO<sub>2</sub>/gelatin. Into a glass beaker was added 99.91 g of a 5 wt% Type 40 gelatin aqueous solution (gelatin solution at 40 °C) and 0.510 g TiO<sub>2</sub> (Unitane). The resulting dispersion was allowed to stir for 15 min. An aliquot of the TiO<sub>2</sub>–gelatin dispersion was puddle deposited onto an unsubbed poly(ethylene terephthalate) (PET) support. A draw bar with a 200 μm gap was used to produce a wet coating of the dispersion on the PET. The coating dried in ambient air, and was removed from the PET, resulting in a free-standing TiO<sub>2</sub>–gelatin film. Horiba analysis found the median TiO<sub>2</sub> particle size to be ~0.480 μm and an XRD experiment confirmed the particles were rutile TiO<sub>2</sub>.

CeO<sub>2</sub>/gelatin. Into a glass beaker was added 99.87 g of a 5 wt% Type 40 gelatin aqueous solution (gelatin solution at 40 °C) and 0.508 g CeO<sub>2</sub> (Aldrich nano <25 nm). The resulting dispersion was allowed to stir for 15 min. An aliquot of the CeO<sub>2</sub>–gelatin dispersion was puddle deposited onto an unsubbed poly(ethylene terephthalate) (PET) support. A draw bar with a 200 μm gap was used to produce a wet coating of the dispersion on the PET. The coating dried in ambient air, and was removed from the PET, resulting in a free-standing CeO<sub>2</sub>–gelatin film. An XRD experiment confirmed the particles were cerianite CeO<sub>2</sub>.

Ag/gelatin. Into a glass beaker was added 99.74 g of a 5 wt% Type 40 gelatin aqueous solution (gelatin solution at 40 °C) and 0.501 g Ag metal powder (Aesar). The resulting dispersion was allowed to stir for 15 min. An aliquot of the Ag–gelatin dispersion was puddle deposited onto an unsubbed poly(ethylene terephthalate) (PET) support. A draw bar with a 200 μm gap was used to produce a wet coating of the dispersion on the PET. The coating dried in ambient air, and was removed from the PET, resulting in a free-standing Ag–gelatin film. Horiba

analysis found the median Ag particle size to be ~24.8 μm and an XRD experiment confirmed the particles were Ag.

**Experimental set-up.** At the Coherence Beamline P10 at the PETRA III synchrotron, the source of X-rays in low-beta configuration was a 5-m-long U29 undulator. The X-rays were monochromatized by a Si(111) double crystal monochromator placed 35 m away from the source. The monochromatic X-ray beam was focused by a pair of K–B mirrors of elliptical shape with a Pd coating. The horizontally focusing mirror (HFM, by JTEC) had a focal length of 200 mm and height errors of 4 nm (peak to valley); the vertically focusing mirror (VFM, by WinlightX) had a focal length of 305 mm, with height errors around 10 nm. The X-ray beam hit the mirrors under a grazing angle of incidence of 4 mrad at the centre; the active length was about 80 mm. At the exit window of the K–B mirror vacuum tank, a coarse W aperture was used to filter only the double-reflected parts of the beam, and suppressed X-rays that hit only one or no mirror at all.

Two tantalum apertures were placed upstream of the focus to reduce the scattering from the K–B mirrors. The focus was measured and tweaked by scanning a crossed pair of 1D X-ray waveguides<sup>33</sup>, by recording the transmitted intensity with a silicon PIN diode (Canberra PD300-500CB), with a thickness of 500 μm and an active area of 19 mm in diameter. Each pair of waveguides consisted of a C guiding layer of 35 nm in thickness, a Mo interlayer and a Ge cladding material; the waveguides were cut to a length of some hundreds of micrometres. Absorbed X-ray photons generate a number of electron–hole pairs of energy 3.66 eV. The resulting charge separation was measured as a current with a picoammeter (Keithley 6485). Two PILATUS detectors were used in two independent experimental configurations. A PILATUS 1M detector with a 981 × 1,043 pixel active area and a total of ten modules was placed at a distance of 167.8 mm downstream of the sample, detecting 13.8 keV monochromatic X-rays. In the second configuration, a 6M detector with a 2,463 × 2,527 pixel active area and a total of 60 modules was placed at a distance of 386.7 mm from the sample, detecting 13.6 keV monochromatic X-rays. The distance between the sample and the detector was calibrated by examining the diffraction patterns of a Ag foil (Supplementary Fig. 1).

**Estimation of the diffraction angle broadening.** The Scherrer equation was used to determine the diffraction angle ( $2\theta$ ) broadening in our experiments<sup>34</sup>,

$$\Delta(2\theta) = \frac{K\lambda}{\tau \cos\theta}$$

where  $\Delta(2\theta)$  is the full-width at half-maximum (FWHM) for the diffraction angle broadening,  $K$  is a shape factor,  $\lambda$  is the wavelength and  $\tau$  is the grain size. In our experiments, the AgBr grain size was measured to be ~700 nm by SEM (Supplementary Fig. 2), but the FWHM of the focused X-ray beam was 370 nm × 270 nm. Thus  $\tau$  of our experiments was determined by the X-ray beam size (~320 nm). Using  $K \sim 1$ ,  $\lambda = 0.9118 \text{ \AA}$  and  $\theta = 0.1944 \text{ rad}$ —corresponding to the Ag(111) spacing of 2.359 Å—we obtained  $\Delta(2\theta) = 0.00029 \text{ rad}$ , from which we estimated the precision in lattice deformation measurements to be  $\Delta(2\theta)/(2\theta) = 7.5 \times 10^{-4}$ .

To experimentally estimate the precision of our lattice spacing measurements, we selected a part of Supplementary Movie 1 (frames #14, #18, #22, #26, #30, #34, #38, #42, #46 and #50—that is, choosing every fourth frame without loss of generality), which shows no observable lattice deformation. We then azimuthally averaged the ten frames to obtain ten 1D curves and used Gaussian fitting to locate the positions of the Ag(111), AgBr(220)/Ag(200), AgBr(200) and AgBr(111) peaks in the curves (where the AgBr(220)/Ag(200) peaks are too close to be distinguished). The mean and standard deviation of the corresponding four peaks in the ten curves were  $2.357 \pm 0.002 \text{ \AA}$ ,  $2.043 \pm 0.003 \text{ \AA}$ ,  $2.887 \pm 0.003 \text{ \AA}$ , and  $3.333 \pm 0.005 \text{ \AA}$ , respectively. The precision of our lattice spacing measurements was determined to be of the order of  $\sim 10^{-3}$ , which is consistent with our calculated value of  $7.5 \times 10^{-4}$  and is about an order of magnitude more accurate than the lattice deformation we measured in our experiments (Fig. 3 and Supplementary Fig. 6). Supplementary Fig. 8 shows an average of the ten 1D curves, which agrees with the known lattice spacings for Ag(111), AgBr(220)/Ag(200), AgBr(200) and AgBr(111).

## References

33. Krüger, S. P. *et al.* Sub-15 nm beam confinement by two crossed X-ray waveguides. *Opt. Express* **18**, 13492–13501 (2010).
34. Patterson, A. The Scherrer formula for X-ray particle size determination. *Phys. Rev.* **56**, 978–982 (1939).